Effect of heat treatment on friction and tribolayer formation in copper

Figueroa, Carlos Gabriel; Schouwenaars, Rafael; Petrov, Roumen; Kestens, Leo

Important note
To cite this publication, please use the final published version (if applicable).
Please check the document version above.

Effect of heat treatment on friction and tribolayer formation in copper

Carlos Gabriel Figueroa [a,c], Rafael Schouwenaars [b,c,*], Roumen Petrov [c,d], Leo Kestens [c,d]

[a] *Departamento de Materiales y Manufactura, Facultad de Ingeniería, Universidad Nacional Autónoma de México, Via de la Innovación 410, PIIT Apodaca, Nuevo León, 66629 Mexico*
[b] *Departamento de Materiales y Manufactura, Facultad de Ingeniería, Edificio O, Universidad Nacional Autónoma de México, Avenida Universidad 3000, Coyoacan, Ciudad de Mexico 04510, Mexico*
[c] *Department of Electromechanical, Systems and Metals Engineering, Ghent University, Technologiepark 903 Zwijnaarde, Ghent 9052, Belgium*
[d] *Department of Materials Science and Engineering, Delft University of Technology, Mekelweg 2, CD, Delft 2628, Netherlands*

ARTICLE INFO

Keywords:
Adhesive wear
Sliding friction
Surface structure
Plastic contact

ABSTRACT

This work analyses the effect of annealing conditions on tribolayer formation in copper under dry sliding conditions. Cold rolled material and samples annealed during 15, 30 and 45 min at 600 °C show an increase in grain size, decrease in hardness and increase in toughness and ductility with time. Electron backscattered diffraction maps describe the severe plastic deformation of a nanostructured tribolayer. Friction coefficients decrease with annealing times, while surface damage diminishes. Wear is lower in the softer material. This is explained by the energy required to produce surface damage, in combination with the energy transmitted to the substrate by friction.

1. Introduction

Heat treatments of metals and alloys are known to impart significant modifications of the microstructure, which are reflected in the mechanical properties of the material. Annealing of cold-worked materials will induce recrystallisation and grain growth [1–3]. During recrystallisation, the cold-rolled microstructure is substituted by fine equiaxed grains. This causes a drastic drop in hardness and a large increase in ductility. Generally, toughness (the area under the tensile curve) increases as well. With increasing annealing times, grain growth occurs, accompanied by a further softening of the material. In earlier work, a significant increase in sliding wear resistance has been observed during the annealing of aluminium, an Al-Sn alloy and copper [4–7]. This effect is investigated into detail here.

Under sliding contact conditions, wear occurs either by oxidative processes or by mechanical modification of the surface [8,9]. Light contact conditions tend to reduce the amplitude of the roughness profile, in a process known as run-in. At higher contact stresses, ploughing may occur [10], resulting in surface plastic deformation. Under critical conditions, small chips of material may be removed in a transition from ploughing to abrasive wear [11]. Adhesion may occur during any of these processes and induces surface damage due to stick-slip conditions or, less commonly, the shearing-off of wear particles. Wear debris often

becomes embedded again in the mating surfaces, leading to the formation of so-called tribolayers and transfer layers [12–14]. Often, a steady state of friction and wear is reached, leading to a considerable increment in roughness [15,16]. Severe plastic deformation (SPD) is observed at the contact surface in a broad set of tribological systems [17].

SPD processes produce nanostructured materials through the increase of dislocation density, with dislocations arranging into subgrain boundaries which become better defined and increase their misorientation as the strain levels increase. The evolution of subgrain boundaries into high angle grain boundaries marks the transition between a highly deformed material and ultrafine or nanostructured materials [18–20]. Ultrafine grained (UFG) and nanostructured materials obtained by classical SPD techniques such as equal channel angular pressing (ECAP) or high-pressure torsion (HPT), often possess high strength but poor ductility [21]. To improve the strength-ductility balance, a grain size gradient can be induced by means of surface severe plastic deformation which improves the tribological behaviour due to the combination of high strength/hardness at the surface and a coarse-grained ductile substrate [22].

Experimental observations [4,23–25] in ductile materials show that sliding wear induces gradients in material, with ultrafine or nano-sized microstructures in the uppermost layers. These have important effects in the tribological behaviour of ductile metals [22]. Rigney described

tribolayer formation as the combination of plastic deformation, material transfer and mechanical mixing [12,13,26]. The deformation process was explained by Kapoor [27–29] as plastic ratchetting during cyclic loading under local intermittent contact. The role of accumulated plastic deformation is illustrated by the observation by Rapoport and co-workers [25,30], who found that a higher stacking fault energy (SFE) lowers the wear rate in FCC-metals, presumably through increased annihilation of dislocations.

Archard's law establishes that wear resistance is proportional to hardness [15], even though the same author expressed doubts about this assumption in a follow-up paper [31]. According to the Hall-Petch relation, a decrease of the wear rate is expected with the reduction of grain size. Although this behaviour has been confirmed for several metallic materials [32–34], it has been observed that the combination of ductility and hardness provides a superior performance under sliding wear conditions [35–38].

Highly ductile materials are not commonly used in wear-sensitive applications, but several exceptions exist, such as journal bearings [23] and electrical contacts in moving components (e.g., heavy equipment in public transportation and electricity generation), where copper alloys are subject to unlubricated wear [39–41]. In previous research, the authors described the microstructural gradient induced by severe surface plastic deformation in pure copper [4], whereas the tribological behaviour and microstructural modifications of ductile materials under sliding contact conditions are described in [5,6].

Here, the effect of annealing time is analysed. Friction and wear are studied using a coaxial tribometer [7]. In addition to the friction coefficient, mass loss and wear track diameter, a description is provided of microstructures, tensile tests, microhardness, crystallographic texture, and surface topography. The discussion focuses on the analysis of the relationship between these data and leads to the conclusion that annealed pure copper presents superior tribological characteristics as compared to the cold worked material; prolonged annealing further reduces the wear rate. The analysis and discussion of the results will focus on the fundamental relationships between tribological behaviour, microstructure and properties obtained using different annealing times.

2. Materials and methods

2.1. Materials

A single commercial slab of electrolytic tough pitch copper was cold rolled to a final reduction of 88% (CR). The central zone of the sheet was cut into four parts, three of which were isothermally annealed at 600 °C during 15 min (15RX), 30 min (30RX) and 45 min (45RX). Prior to the tribological tests, the Cu surfaces were prepared by conventional mechanical polishing to a surface root mean square roughness (R_{RMS}) of 0.65 ± 0.03 μm. Processing conditions and initial mean roughness values are summarised in Table 1.

Four tensile tests were performed on each material on subsize specimens as prescribed in ASTM E8 [42]. In addition to the 0.2% proof stress ($\sigma_{0.2}$), ultimate tensile stress (σ_{Max}) and maximum elongation (ε_{Max}), the toughness (T) of the material was determined by numerically integrating the area below the tensile curve until fracture. Confidence intervals were calculated using *t*-statistics [43]. A 90% confidence

interval (two-sided) is used for all values. Tensile results are presented in Table 2.

Four tribometer tests were performed for each condition using a coaxial tribometer described in [7], without lubrication at room temperature and ambient atmosphere. The test consists in applying a 100 N constant normal load by means of a cylindrical pin with spherical cap of 200 mm radius produced from non-quenched AISI9840 steel (hardness of 2900 MPa) on Cu-coupons of 20 mm × 20 mm. The pin rotates around its own axis at a constant angular speed of 60 rpm for 300 s. Normal load and rotating speed are measured and controlled by means of a dynamic feedback system and torque is measured synchronously. Pins are cleaned and repolished after each test and substituted if surface damage is observed.

2.2. Friction coefficients

A scheme of the coaxial tribometer is presented in Fig. 1. Normal load (N), torque (T), and velocity are measured synchronously. Although no friction coefficients were provided in earlier work using this equipment [4–7,44,45], approximate values can be obtained by measuring the wear track diameter.

While Amontons' second law states that the friction force is independent from the apparent contact area, this is not the case for the torque T in the present configuration. For a contact radius *a* and an a-priori unknown pressure distribution $p(r)$, the normal load N and torque T are given by:

$$N = \int_0^a p(r)2\pi r dr \tag{1}$$

$$T = \int_0^a \mu p(r)2\pi r^2 dr \tag{2}$$

For a perfectly plastic material, one may assume that the material flows to achieve a uniform pressure distribution in the contact zone. Integration of (1) provides the value of *p*, which can be substituted in (2) to obtain an estimated value of the friction coefficient μ_{pl}:

$$\mu_{pl} = \frac{3T}{2aN} \tag{3}$$

On the other hand, for a perfectly elastic material, the pressure distribution is Hertzian [11]:

$$p(r) = \frac{3N}{2\pi a^2}\sqrt{1 - \frac{r^2}{a^2}} \tag{4}$$

Substituting in (2) allows to calculate the friction coefficient μ_{el}:

Table 2
Tensile properties.

Specimen designation	$\sigma_{0.2}$ (MPa)	σ_{Max} (MPa)	ε_{Max} (%)	T (MJ/m³)
CR	471 ± 38	609 ± 24	3 ± 0.3	13 ± 1
15RX	115 ± 7	415 ± 22	28 ± 1	94 ± 7
30RX	103 ± 7	417 ± 26	32 ± 4	112 ± 9
45RX	111 ± 6	432 ± 21	31 ± 4	112 ± 16

Table 1
Processing conditions and roughness prior to the tribological test.

Specimen designation	Specimen conditions				Tribological test parameters			
	Reduction (%)	Annealing temperature [°C]	Annealing time [s]	Initial R_{RMS} μm	Angular speed. [RPM]	Normal load [N]	Testing time [s]	Pin
CR	88	N/A	N/A	0.62	60	100	300	AISI9840
15RX	88	600	900	0.68				
30RX	88	600	1800	0.66				
45RX	88	600	2700	0.64				
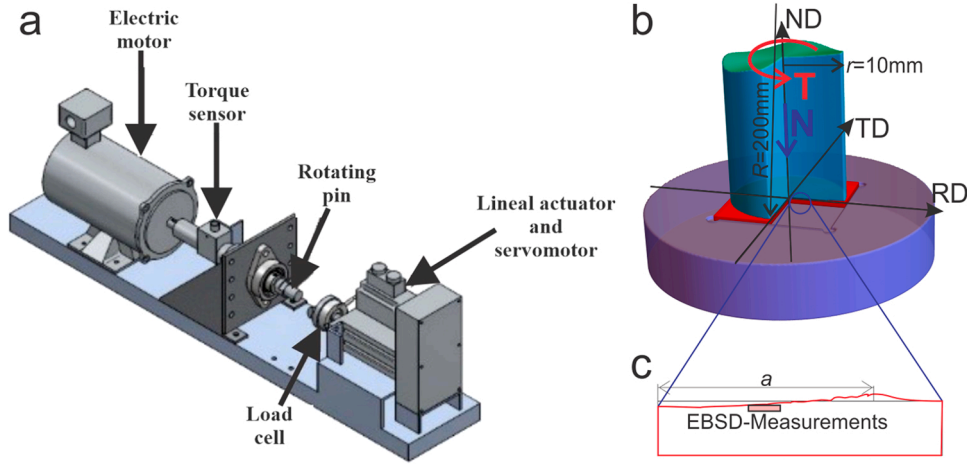
Fig. 1. a) Coaxial tribometer assembly, b) Schematic representation of pin and sample geometry, with a cut-out to show the measuring zone for EBSD (c). Notice that the vertical profile in (c) is strongly exaggerated. T: torque, N: normal load, RD: sample rolling direction, TD: sample transverse direction, ND: sample normal direction, *r*: pin radius, *R*: contact surface radius, *a*: wear track radius.

$$\mu_{el} = \frac{16T}{3\pi a N} \approx 1.7\frac{T}{aN} \tag{5}$$

It follows that μ_{el} is only 13% higher than μ_{pl}. Evidently, Hertzian contact does not occur in the tests on ductile materials. Eq. (5) provides an upper bound for the friction coefficient. The fact that it is close to the ideally plastic case shows that a friction coefficient can be reasonably estimated in the experiments. An average value (1.6 *T/aN*) will be reported here, accepting an uncertainty of ± 6.5% due to the unknown pressure distribution. An additional assumption in these calculations is that *a* is a constant. From tests on a wide range of ductile materials and in absence of severe abrasive or adhesive wear, this is approximately true after the first 5–15 s of the test. The friction coefficients reported here should be interpreted as qualitative data which can be compared between tests performed under identical conditions on similar materials.

2.3. Specific wear rate and wear coefficients

The specific wear rate is defined as:

$$w_s = \frac{\Delta m}{\rho N s} \tag{6}$$

where Δm is the mass loss, ρ the density of the worn material (8960 kg/m^3) and *s* the sliding distance [46]. With the angular velocity $\dot{\omega}$ (in RPM) and test time *t* (s), an equivalent sliding distance can be defined as:

$$s = \frac{2\pi\dot{\omega}t}{60}\frac{1}{a}\int_0^a r\,dr = \frac{\pi\dot{\omega}t}{60}a \tag{7}$$

Hence:

$$w_s = \frac{60}{\pi\dot{\omega}t}\frac{\Delta m}{\rho Na} \tag{8}$$

Archard's equation [15] can be written in terms of mass loss:

$$\Delta m = K\frac{3\rho N s}{H} \tag{9}$$

Where *H* represents the hardness of the material. This equation is the basis of the assumption that hardness is directly related to wear resistance.

The product μNs, with μ the friction coefficient, is the work transferred from the pin to the worn material [47]. Reye, long before Archard [48], postulated that wear would depend on the amount of energy required to remove material (See also Scherge et al. [49] and

Shakhvorostov [50] et al.). Archard considered the approximate relationship between the flow strength of a material and the hardness [51] to introduce 3*H* in Eq. (9). Similarly, one can use the toughness *T* as a first approximation for the energy required to produce failure in a ductile material. This allows to define two distinct, non-dimensional wear coefficients, K_H based on hardness and K_T based on energy:

$$K_H = \frac{\Delta m H}{3\rho N s} = \frac{H}{3}w_s \tag{10}$$

$$K_T = \frac{\Delta m T}{\mu\rho N s} = T\frac{w_s}{\mu} \tag{11}$$

The values of both coefficients will be discussed briefly in Section 3.2.

2.4. Characterisation

The surface roughness was characterised before and after the test by means of a Nanovea optical profilometer using Chromatic Confocal Technology. To determine roughness values, the built-in software fits a 6th degree polynomial to the measured surface; deviations from this fitted surface are then characterised as roughness. Worn surfaces were observed using a Philips XL20 scanning electron microscope (SEM).

To characterize microstructural changes induced during the tribological process, sections were prepared trough the centre of the wear track by conventional metallographic techniques. Images are presented with the rolling direction along the horizontal line and the normal direction vertical.

Friction coefficients, wear track diameters and mass loss were determined for all 4 samples tested. Roughness maps, SEM-observation and microstructure/microtexture determination were performed on a single specimen for each material.

The worn microstructures were analysed by electron backscatter diffraction (EBSD) using a FEI Quanta 450 SEM with a field emission gun operating at 20 kV and a beam current of 2.4 nA. The orientation data were acquired with EDAX-TSL Data collection V7 software in hexagonal scan grids with step size of 100 nm for the original material, while for the worn samples, the step size was 55 nm. Orientation data were post-processed with the MATLAB™ toolbox MTEX version 5.1.1 [52].

Hardness measurements were executed using a Nanovea platform with a Vickers indenter applying a maximum load of 0.5 N with a holding time of 10 s. Loading and unloading rates were 0.25 N/min and 1 N/min, respectively. Eight measurements were performed on each sample before the wear test. The highest and lowest value of each set

was discarded, resulting in a total of 24 hardness values for each material condition.

2.5. Grain size, grain size distribution and orientation distribution functions

Under the classical approach for quality control in 20th-century mechanical and metallurgical engineering, grain size is a number [53], determined by relatively simple measurements on a limited number of grains. Modern image acquisition and analysis techniques allow measuring thousands of grains which permits determining the entire grain size distribution. Because the uncertainty on the estimation of a sample mean decreases according to $n^{-1/2}$, with n the sample size [43], these techniques determine the average grain size with extreme precision.

Grain size distributions were determined from the EBSD-data in two manners. One method is to use the smooth kernel distribution, in which each grain is modelled by a narrow probability distribution function (PDF, e.g. Gaussian) centred on the size of each measured grain, with a weight of $1/n_g$, n_g being the number of grains. This method critically depends on the choice of the kernel width [54]. The second method is to fit a parametric statistical distribution to the empirical cumulative distribution function (EDF) of the data and plot the corresponding PDF. The two-parameter gamma distribution was used here. Fitting a smooth distribution to an EDF unavoidably erases all fluctuations but emphasizes the general trend.

Although statistical tests can be devised to verify whether two distribution functions are significantly different, the law of large numbers (>1900 grains measured in each microstructure) makes such tests superfluous. Likewise, if the ODF-plots show clear differences in visual appearance, the distributions are significantly different [55,56].

3. Results

3.1. Surface modification

Fig. 2 shows representative topographies of each worn surface. Fig. 2a corresponds to CR. Wear debris is trapped in the centre of the track, the negative topography around the centre corresponds to material removal. In annealed materials, the centre of the track is relatively smooth, as the material conforms to the geometry of the pin. Material is drawn into the sliding direction, as can be seen more clearly in Fig. 2c, where a wear flake is forming. Simultaneously, the material is pushed outward to form a rim around the centre of the track.

Fig. 3 presents SEM images of worn surfaces for each condition. Fig. 3a. (CR) shows clear grooves which may point to abrasive wear, a few particles of wear debris (WD) embedded in the surface and some spots which may be associated to adhesive wear (AW). Worn surfaces 15RX, 30RX and 45RX are presented in Fig. 3b, c and d, respectively. Adhesive wear is visible, in the form of surface flakes which are drawn into the sliding direction and leaving surface cracks behind. The intensity of this phenomenon increases with increasing grain size. No evidence was present of copper being transferred to the pin.

3.2. Friction and wear parameters

Fig. 4 shows the friction coefficients during the tribometer tests. The four individual curves and an average curve are presented. The overall mean (i.e. averaged over 300 s) is shown as a black line, with dashed lines indicating the 90% confidence band for the overall mean. A clear reduction in the friction coefficient and its variation during the test is seen from CR to RX15 and then RX30. The small increase in μ and its standard deviation from RX30 to RX45 is insignificant, as the average value of either sample is within the confidence band of the other.

The friction coefficient, diameter of the wear track and mass loss are plotted against hardness in Fig. 5. The friction coefficient and mass loss
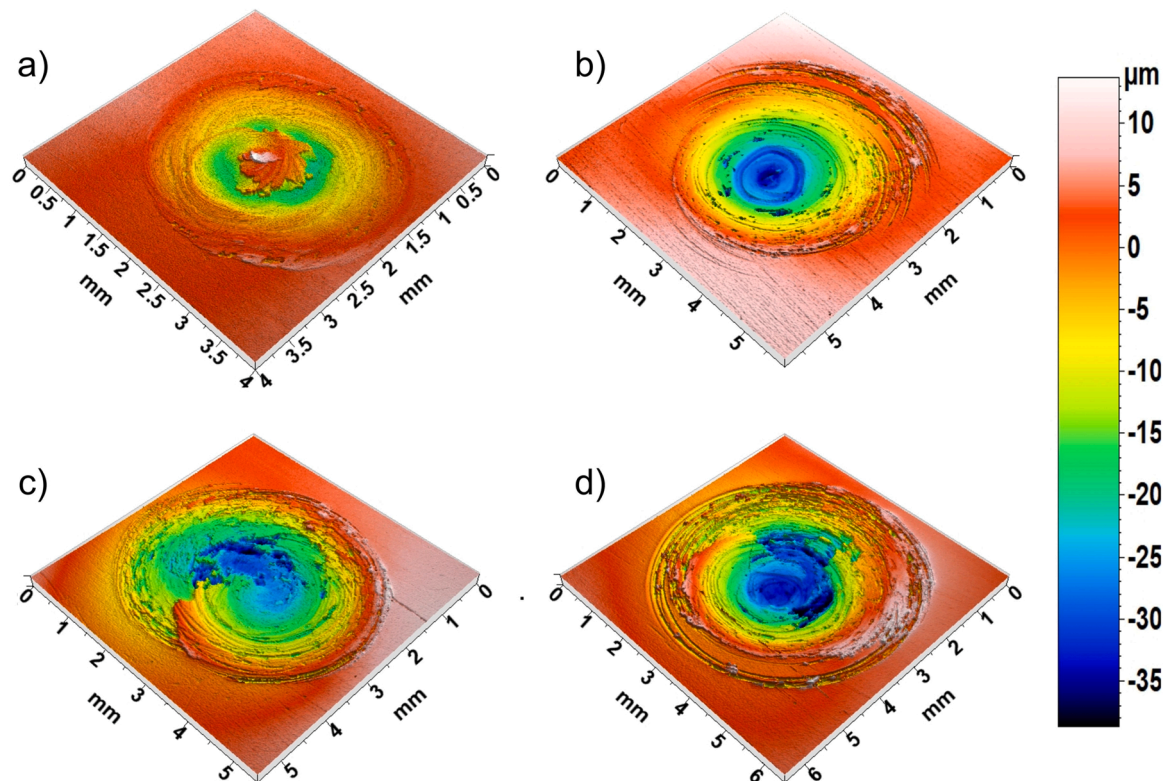

Fig. 2. Representative topographies of each material after the test. a) CR, b) 15RX, c) 30RX and d) 45RX.
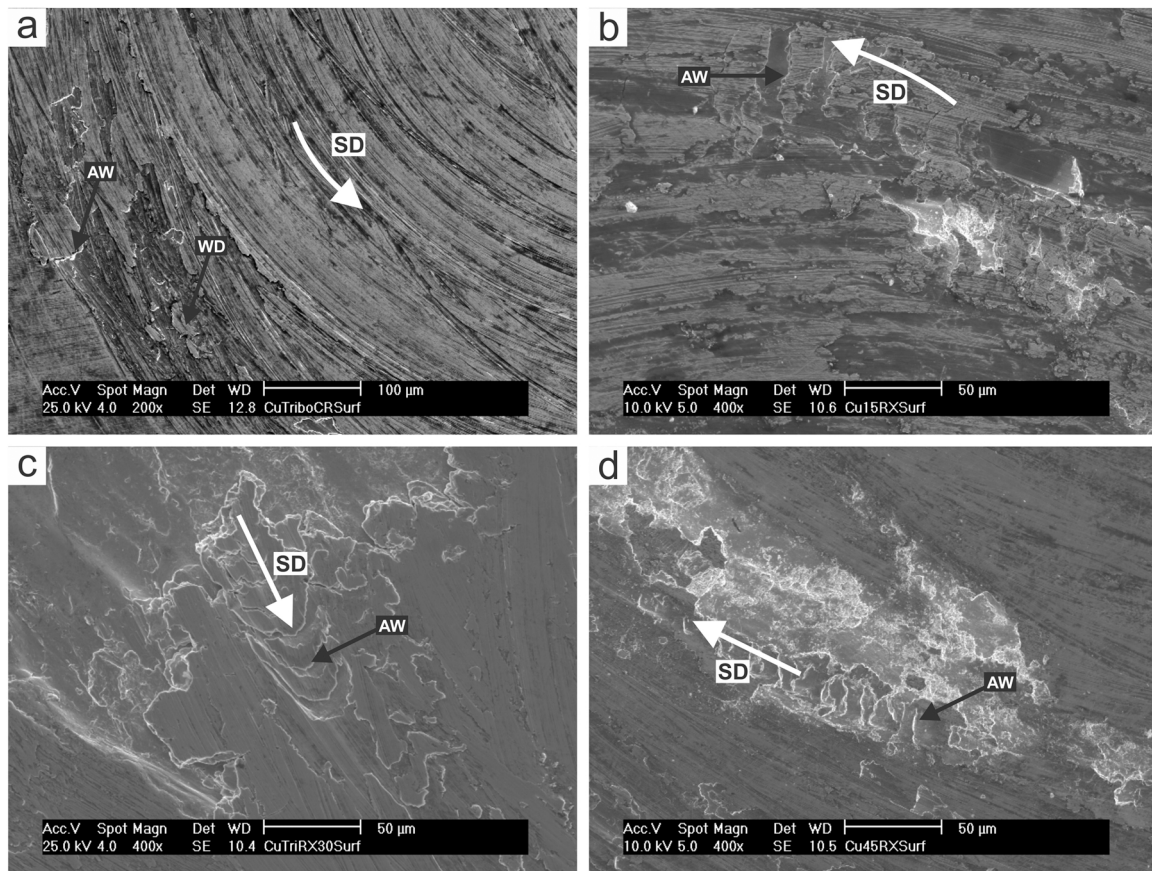
Fig. 3. SEM images of worn surfaces showing adhesive wear signs. a) CR, b) RX15, c) RX30, d) RX45. AW=Adhesive wear, WD=Wear debris, SD=Sliding direction.

increase with hardness (i.e. decrease with grain size or annealing time). The wear track diameter increases as the hardness decreases, due to increased plastic deformation. The wear coefficients K_H and K_T are plotted against H/E in Fig. 6. It shall be noted that Young's modulus for Cu (117 GPa) does not depend on heat treatment, but has the advantage of being non-dimensional, like K_H and K_T. The values of the wear parameters are summarised in Table 3.

3.3. Initial microstructures and crystallographic textures

The EBSD scans of the starting microstructures are shown in Fig. 7. Fig. 7a presents the microstructure of cold rolled material with the typical elongated grains, whereas b), c) and d) show recrystallized microstructures with annealing twins.

Fig. 8 shows the ODFs calculated for each annealing condition. Fig. 8a presents the most important sections of Euler space for the crystallographic texture of CR, showing a well-known texture, with the Copper ({112} <111 >) and S ({123} <614 >) components connected with the Brass ({011} <211 >) orientation, defining the β-fibre characteristic for copper [54–56]. The annealed specimens show a strong Cube ({001} <100 >) component with the presence of the {122}< 212 > orientation which is associated to annealing twins; a low-intensity β-fibre is retained from the rolling texture and decreases in intensity as annealing time increases.

The grain size distribution in annealed material before testing is shown in Fig. 9. A systematic shift of the grain size to the right corresponds to the natural process of grain growth at elevated annealing temperatures. The bimodal character in the smooth kernel distribution for RX45 may indicate the onset of abnormal grain growth [2,3]. In the cold-rolled structure, grain boundaries are a mixture of high-angle grain boundaries and newly formed low-angle and high-angle grain

boundaries [2,3,18,20,21,57,58]. This gradual break-up of the original microstructure means that a unique definition of a grain size is not possible, as can be concluded from Fig. 6a as well. Grain sizes before and after testing are reported in Section 3.4 (Table 4).

3.4. Microstructures and crystallographic textures of worn material

The IPF-maps of worn material 10 μm below the sliding surface are shown in Fig. 10. The upmost zone of the worn material does not produce identifiable EBSD-patterns, as the grains are too small, and the lattice may be distorted by incorporation of oxygen or other impurities induced during the wear test [59]. The grain fragmentation, formation of high angle grain boundaries and ultra-fine grained structures typical for the SPD-processing of copper are evident [4,60–62].

The surface strain mode during sliding contact is expected to be close to simple shear. Stable crystal orientations observed in FCC materials subject to simple shear [63–65] are shown in Fig. 11, which also presents the experimental ODFs obtained from the IPF-maps shown in Fig. 10. CR, RX15 and RX30 show relatively weak textures with the main components slightly off the ideal positions on the α-fibre; the same components are found in RX45 but with a higher intensity.

The grain size distributions of the modified surface layers are shown in Fig. 12. The grain refinement is obvious by comparing to the scale of the ordinate axis in Fig. 9. A summary of grain sizes before and after the test are shown in Table 4. There is a clear variation from CR to RX45, with a stronger grain refinement in materials with smaller grains in the starting microstructure. This is indicated by the refinement factor, defined as the initial size divided by the final size.
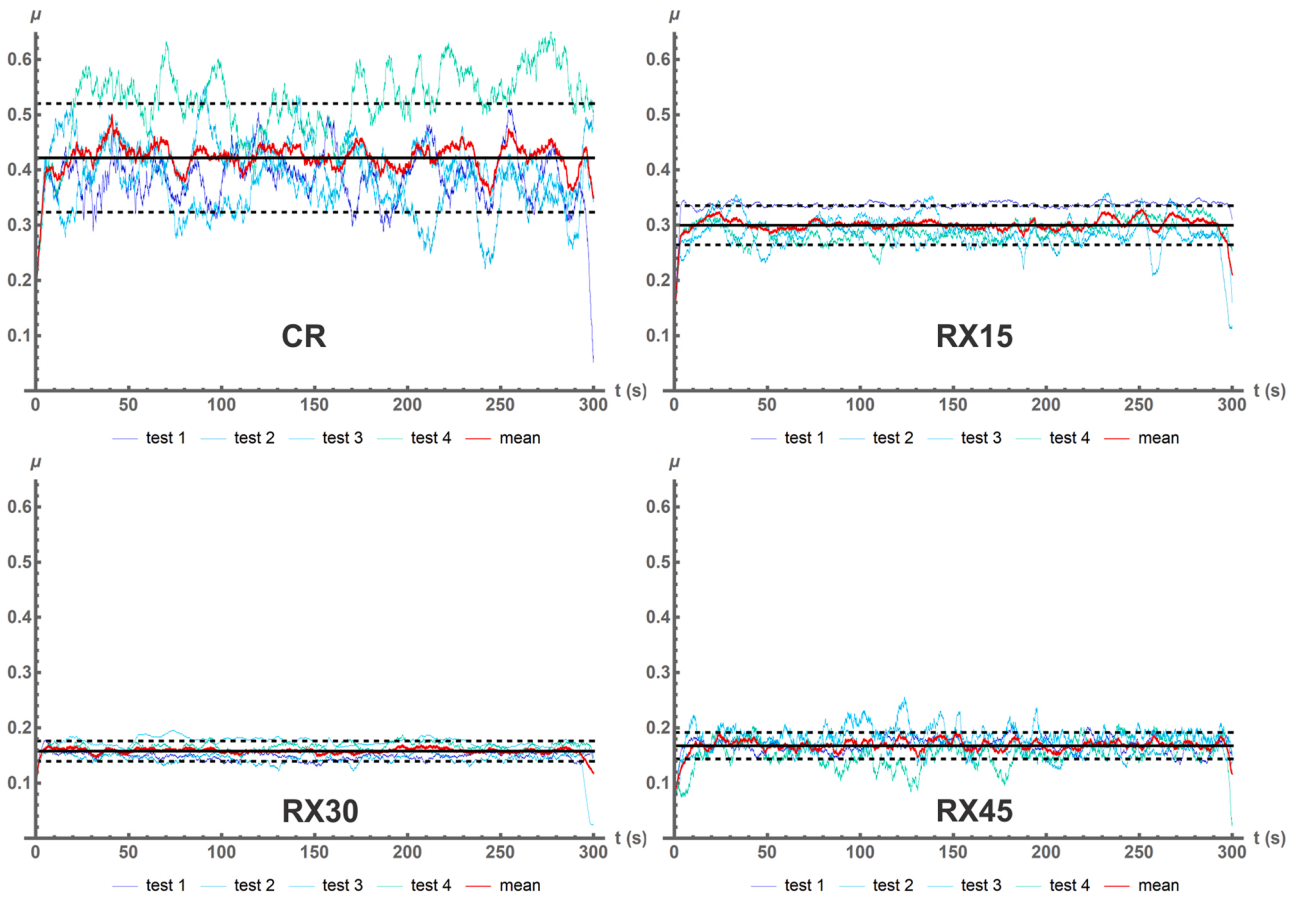
Fig. 4. Friction coefficients for the four materials. Green-blue lines indicate the individual tests. The red line shows an average curve, the black horizontal line is the overall average (averaged over 300 s) with the 90% confidence band indicated by dashed lines.
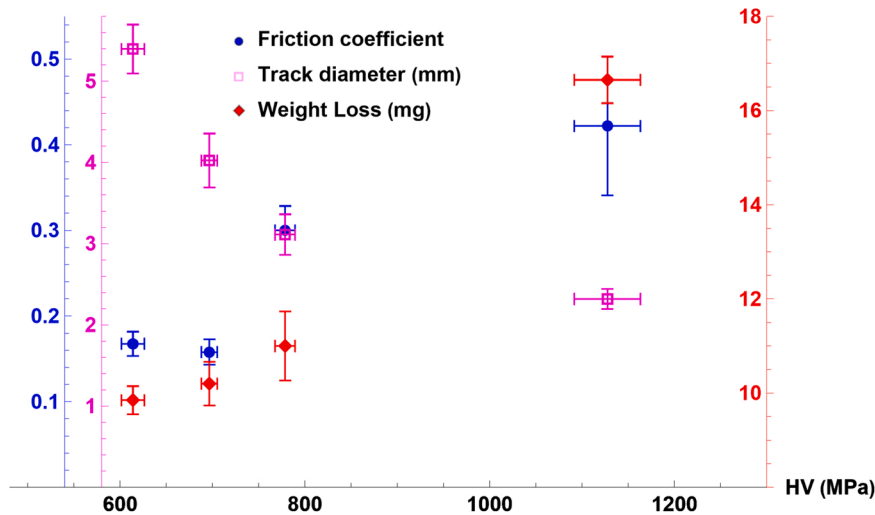

Fig. 5. Chart of friction coefficient, wear track diameter and specific wear rate vs. indentation hardness of the material before testing.

4. Discussion

4.1. Analysis of textures, microstructures and worn surfaces

In a previous paper [4], the authors presented an in-depth analysis of the texture and microstructure gradient developed in the CR and RX45 material. It was shown that, in the CR-material, the subsurface zone is subject to a static recrystallisation process due to accumulated strain energy. This recrystallised structure is then further refined by the SPD process. Both in CR and RX45, the final grain subdivision is produced by concurrent recrystallisation and severe plastic deformation. The present work considers intermediate annealing times and focuses on the tribological aspects of these processes.

Determination of mechanical properties and tribological parameters require simple sample preparation and short measuring times as compared to the detailed microstructural characterisation of
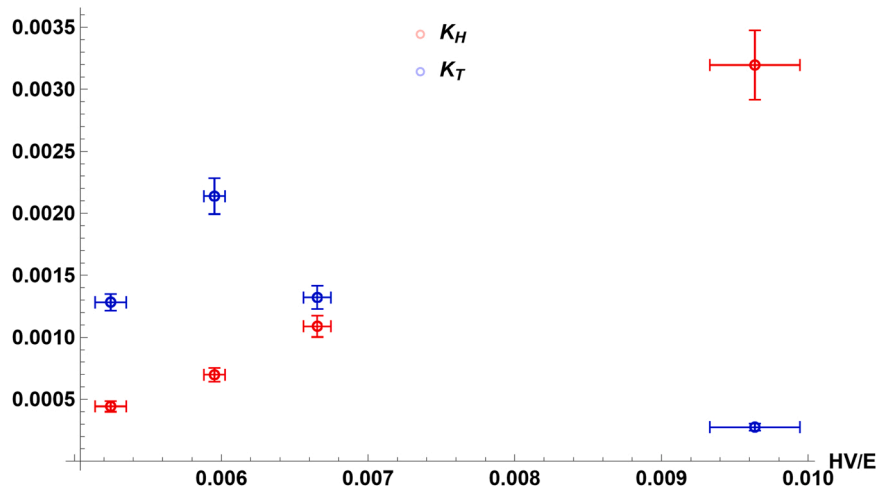
Fig. 6. Wear coefficients K_H and K_T as a function of H/E. Both coefficients show significant variations between the four materials tested.

Table 3
Hardness, average wear track diameter, root mean square roughness, friction coefficient, mass loss, specific wear rate and wear coefficients for each material.

	CR	15RX	30RX	45RX
Initial hardness (MPa)	1127 ± 36	778 ± 11	696 ± 9	614 ± 12
Track diameter (mm)	2.3 ± 0.1	3.1 ± 0.2	4 ± 0.3	5.4 ± 0.3
Final R_{RMS} (μm)	4.7	2.09	1.64	1.34
Friction coefficient	0.42 ± 0.08	0.30 ± 0.03	0.16 ± 0.01	0.17 ± 0.01
Mass loss (mg)	16.6 ± 0.5	11.0 ± 0.7	10.2 ± 0.5	9.9 ± 0.3
Specific wear rate (10^{-12} m^2/N)	8.5 ± 0.6	4.2 ± 0.2	3.0 ± 0.1	2.1 ± 0.1
Wear coefficient (Hardness) K_H ($\times 10^{-3}$)	3.2 ± 0.3	1.0 ± 0.1	0.60 ± 0.05	0.44 ± 0.04
Wear coefficient (Toughness) K_T ($\times 10^{-3}$)	0.28 ± 0.03	1.3 ± 0.1	2.1 ± 0.1	1.31 ± 0.06

nanostructured materials, whether by EBSD or transmission electron microscopy. A fundamental insight in the mechanisms of friction and wear of metallic materials cannot be achieved without such analysis [4, 12,14,23–25,30,66]. The analysis of crystallographic texture is only slowly being incorporated in the study of wear mechanisms [67–69]. EBSD measurements provide high-resolution images of the ultrafine microstructure while texture evolution is related to the plastic strain modes and the micromechanical effects involved in the deformation process [70].

The geometry of the test suggests that the strain mode is simple shear, as confirmed by the ODFs shown in Fig. 11. The measured components are slightly shifted with respect to the ideal orientations, due the outward flow of metal which produces the rim around the wear track. A prominent feature of the ODFs presented in Fig. 11 is that the textures are weak, except for RX45, which resemble textures measured and predicted in torsion for "conventional" strain levels [71,72].

For the other three conditions, the textures are like the ones obtained in HPT or ECAP of copper [73–77]. This weakening of the texture has not been explained completely to date. The strong difference between RX45 and the other materials suggests that the latter has not yet reached this critical level of grain subdivision after 300 s

The worn surfaces show a systematic transition as well. CR shows a pattern of concentric grooves with some evidence of small wear particles. RX30 and RX45 present evidence of surface material dragged along with the pin due to adhesion. This behaviour is consistent with the hardness of these materials. The harder material will be more prone to fracture and produce debris which can damage the surface. The softer

material tends to flow and, if debris is generated, it can be incorporated in the tribolayer more easily.

The grain size distributions after tribological modification (Fig. 12) reinforce the idea that all four materials represent distinct stages of a single refinement process, which takes longer when starting with a coarser microstructure. The role of the friction coefficient and hardness in this evolution will be analysed in the following subsection.

4.2. Analysis of the relationship between hardness and friction coefficient

From a theoretical viewpoint, the tangential force caused by friction is the derivative of frictional work with respect to the sliding distance. Mating copper with steel, chemical adhesion forces are supposed to be low [78]. Therefore, differences in friction coefficients observed reflect the energy of the mechanical processes associated to wear. During the last decade, a better understanding has been established of the relationship between the interaction of asperities and contact spots at the surface and the plastic deformation of the subsurface layer. Experimental observation of ploughing, folding and cutting by a sliding wedge [79–81] confirm and refine the mechanisms predicted in early work on the wear of ductile materials [10,11]. Finite element models [82] and large-scale molecular dynamics simulations [83] have elucidated the shear instabilities which accompany the SPD-processes responsible for subsurface nanostructuring.

The work required for these mechanisms is proportional to the yield strength of the material (and consequently to the hardness). Under identical test geometries and assuming ductile behaviour, a harder material will require more work to induce these phenomena and therefore present a higher friction coefficient. Most of this work is transformed into heat due to the plastic dissipation, although a small fraction is retained as internal energy in grain boundaries and dislocation networks [1–3]. This provides a possible explanation for the slower microstructural evolution in the softest material.

4.3. The role of ductility in mass loss

Large-scale molecular dynamics simulations [8] have shown that under most conditions, asperities have the tendency to deform plastically and become incorporated in the surface layer, rather than being sheared from the surface. The shearing-off of asperities forms the basis for Archard's wear model. It is clear, both from advanced simulations [8, 82–86] as from the experimental evidence, that this mechanism is not important for ductile materials. For the materials studied here, mass loss, the specific wear rate w_s and the hardness-based wear coefficient K_H strongly decrease as hardness decreases, demonstrating that for ductile
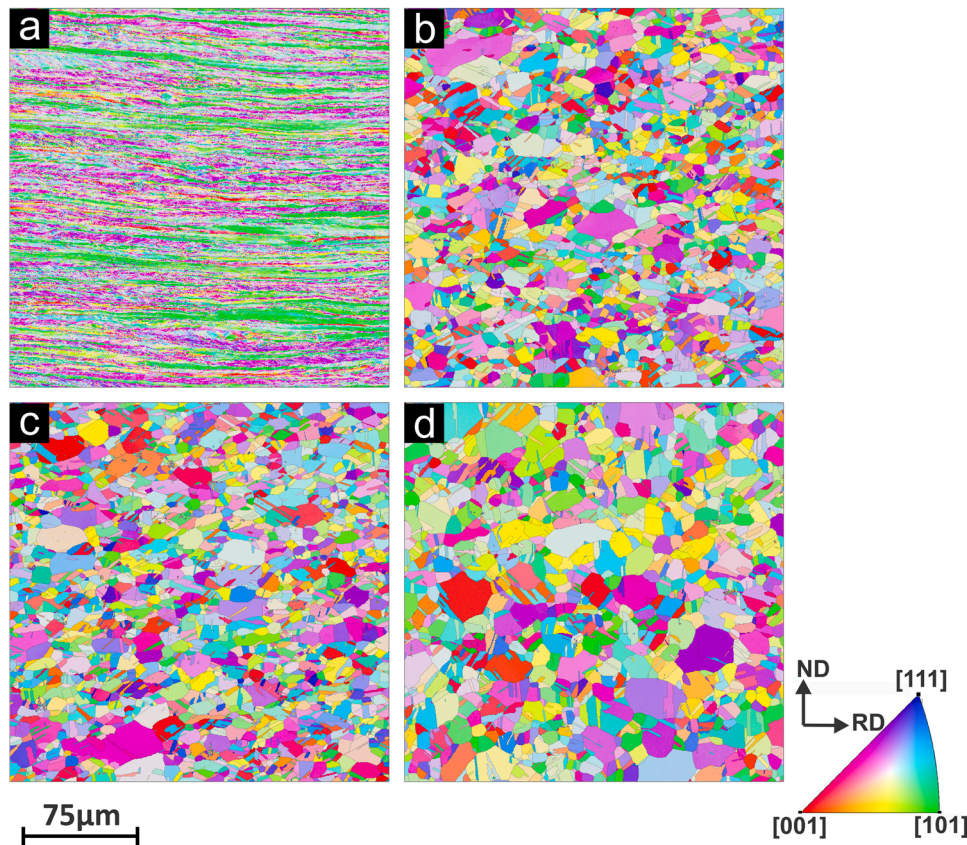
Fig. 7. Inverse Pole Figure Maps (IPF-maps) of the starting material. a) CR, b) RX15, c) RX30, d) RX45 (RD: horizontal, ND: vertical).

materials, hardness does not improve wear resistance.

The toughness-based wear coefficient K_T was proposed to verify if wear resistance can be related to the energy required to remove wear debris, as may be expected for ductile failure. K_T shows considerable variation as well, indicating that this approach is an oversimplification too. It can be argued that the strain mode during wear is significantly more complex than in a tensile test. However, it is the authors' opinion that the variation of microstructures induced by thermal treatments and the complexity of the microstructural evolution during wear are too complex to be characterised by a single constant such as K_H or K_T.

4.4. The role of energy

Although toughness itself could not provide a clear link to the mass loss in this study, the energy-based approach allows to make a connection between the wear characteristics and the differences in microstructure and crystallographic texture. For the harder material, more work is required to overcome friction. More work is therefore transmitted to the substrate and surface modification is faster. The softest material (RX45) accommodates more easily to the geometry and local roughness of the contacting body. Consequently, less work is applied, and microstructural modification is slower. This can explain the notable differences in texture evolution and the systematic variation of the grain size distributions shown in Figs. 9 and 12. Apparently, the amount of energy provided through friction is more important than the amount of energy required to remove debris, for the materials and wear conditions studied here.

5. Conclusions

Microstructural modification and surface damage were analysed in a sliding wear test on cold rolled and recrystallised copper with three different annealing times. The friction coefficient and mass loss increase with the hardness in the four samples, while the wear track diameter increases as the material becomes softer, due to the increased plastic deformation of the material under the pin.

Grain refinement and modification of the crystallographic texture in the four materials appear to represent different stages of the same process. The texture in the coarse-grained sample does not yet show the weakening which is typically observed in SPD-processed FCC-materials. This difference in evolution rate was associated to the differences in friction coefficients.

Earlier work indicated that sliding wear in ductile materials is associated to the amount of frictional work that can be absorbed in the form of plastic deformation before material loss occurs. Consequently, well-annealed materials are expected to have a longer lifetime than cold worked metals. The present work adds a new aspect to this observation, in the sense that the friction coefficient is smaller in well-annealed materials. Ploughing, folding, and cutting, causing material loss in the cold rolled material require more work than the occasional adhesive contact in a soft and ductile material.

The severe modification of the subsurface layers indicates that most frictional energy is dissipated through plastic deformation. The material with higher friction coefficient will accumulate plastic deformation more rapidly, explaining the different rates at which the SPD-process occurs in the four materials tested here. Then, the softest materials, with the lower friction coefficient, have the highest wear resistance. Neither hardness nor toughness can be used as a single parameter to characterise the wear resistance in cold rolled and annealed copper, but the energy-based reasoning provides a basis to explain the microstructural and microtextural evolution observed in this study.
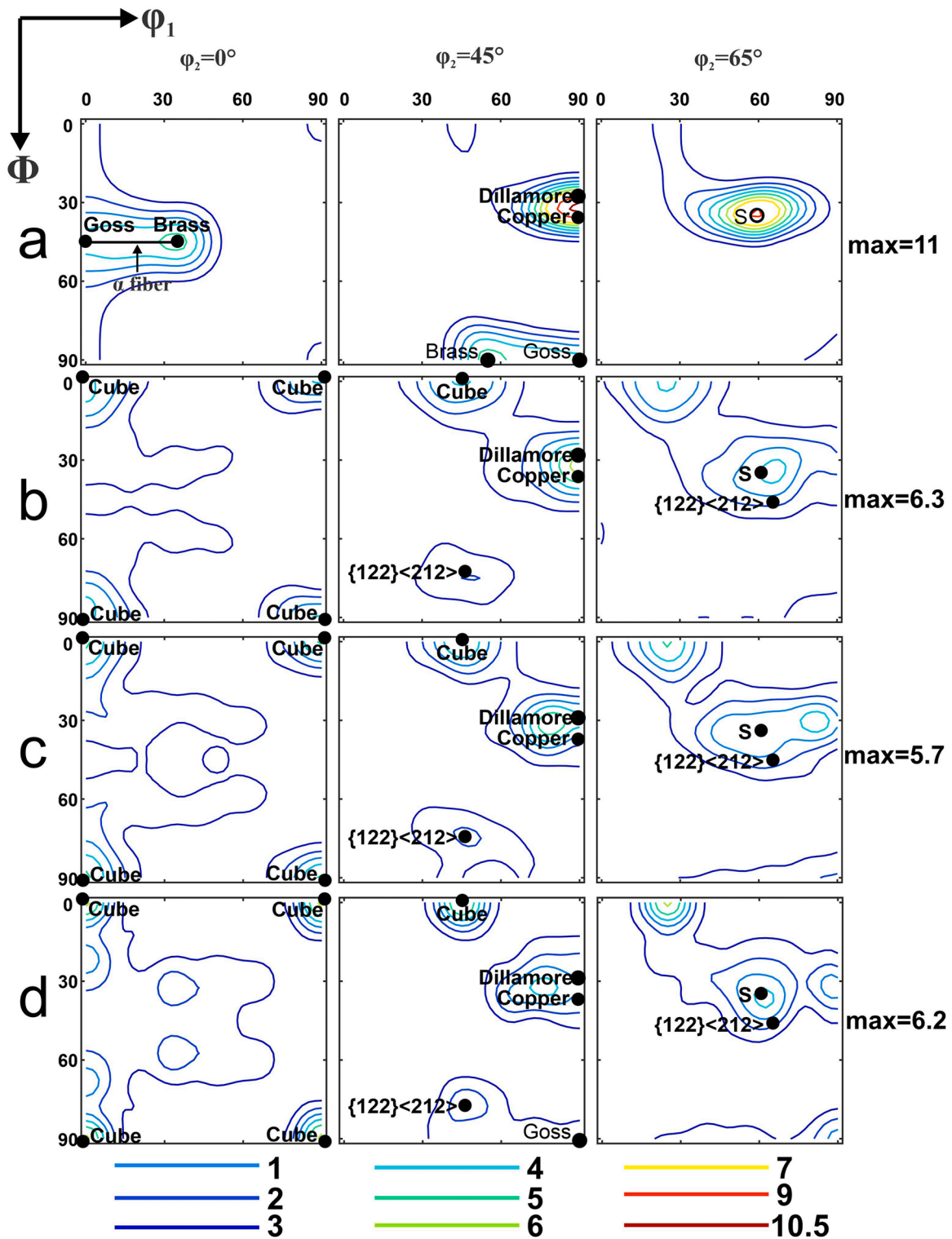
Fig. 8. ODF sections ($\varphi_2 = 0°$, $45°$, $65°$) of the material before the tribological test a) CR, b) RX15, c) RX30, d) RX45.

Declaration of originality

- Many investigations on friction and wear still focus on surface observation alone and use measurements of weight loss, roughness and friction to characterise wear progress. This work presents an integrated approach in which such classical tribological measurements are connected to the subsurface modification and mechanical properties of the material.

- The novelty of the paper resides in the connection that was made between the metallurgical mechanisms of tribolayer formation (severe plastic deformation, recovery, recrystallisation) and the kinetics of friction and wear under unlubricated sliding conditions. The incorporation of detailed microtexture measurements in the study of wear in a classical reference material (electrolytic copper) is still a relatively new approach and contributes interesting information on
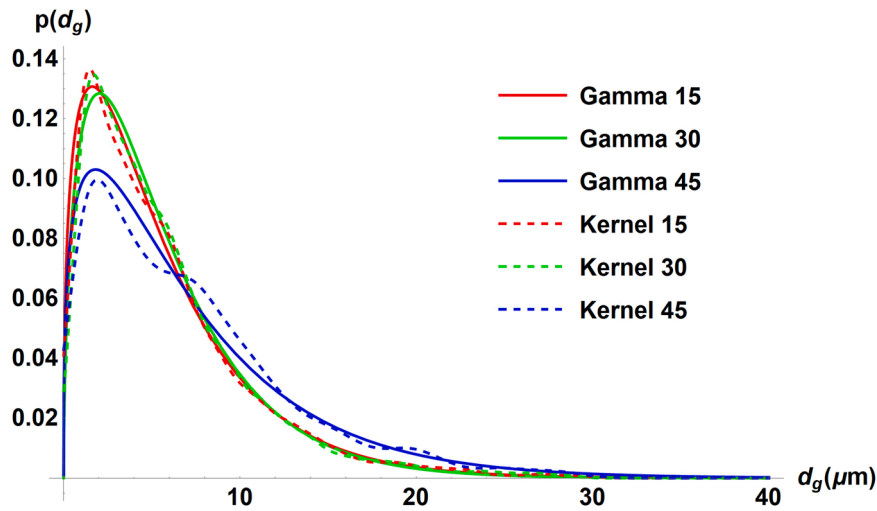
Fig. 9. PDF of the original grain size distribution. "Gamma" indicates the PDFs obtained by fitting the cumulative gamma distribution to the empirical CDF, "Kernel" corresponds to the smooth kernel distributions, for 15, 30 and 45 min of annealing.

Table 4
Average grain size before and after the test, and the relation between both values (refinement factor).

Material	CR	RX 15	RX 30	Rx 45
d_g **Initial (μm)**		5.6	5.7	7.0
d_g **Worn (μm)**	0.40	0.50	0.55	0.71
Refinement factor		11.2	10.4	9.8

how the annealing state of this material affects friction, wear and subsurface modification.

- The notice that hardness is not a determining factor in the sliding wear of ductile alloys is reinforced. As annealing time is increased and hardness reduced, the wear velocity is significantly reduced. A wear coefficient based on Archard's equation does not capture the wear resistance of this set of materials. It is shown that the wear velocity is both affected by the amount of frictional energy injected into the system and the amount of plastic energy required to remove wear debris, but a wear coefficient based on material toughness is also not capable of characterising the complex processes observed using a single parameter.
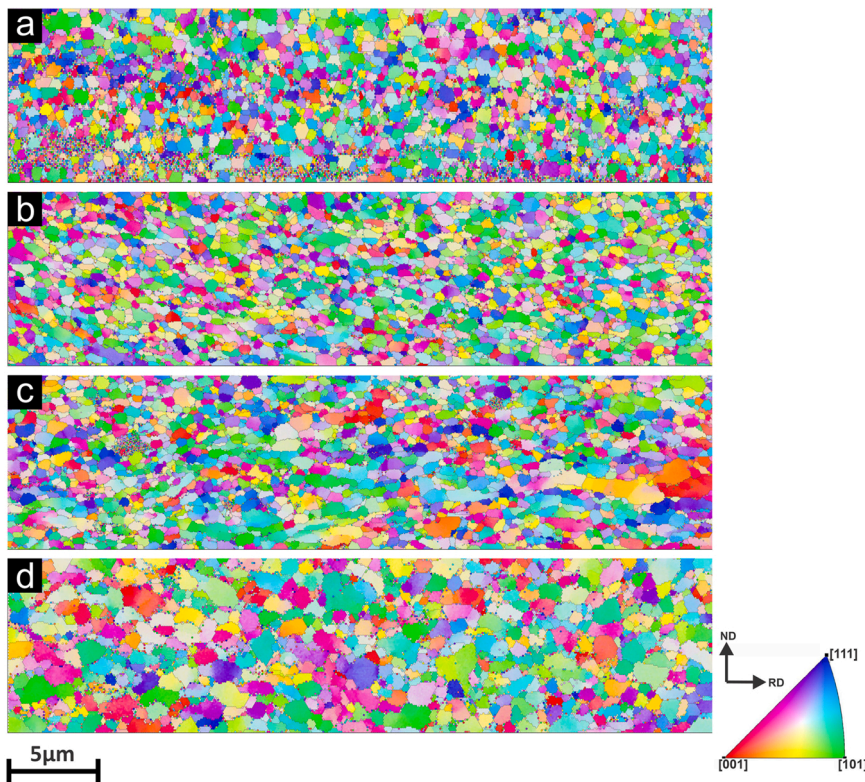

Fig. 10. IPF-maps obtained after the tribological test for a) CR, b) RX15, c) RX30, d) RX45. The centreline of each micrograph is 10 μm below the surface. (RD: horizontal, ND: vertical, sliding direction perpendicular to image, see Fig. 1).

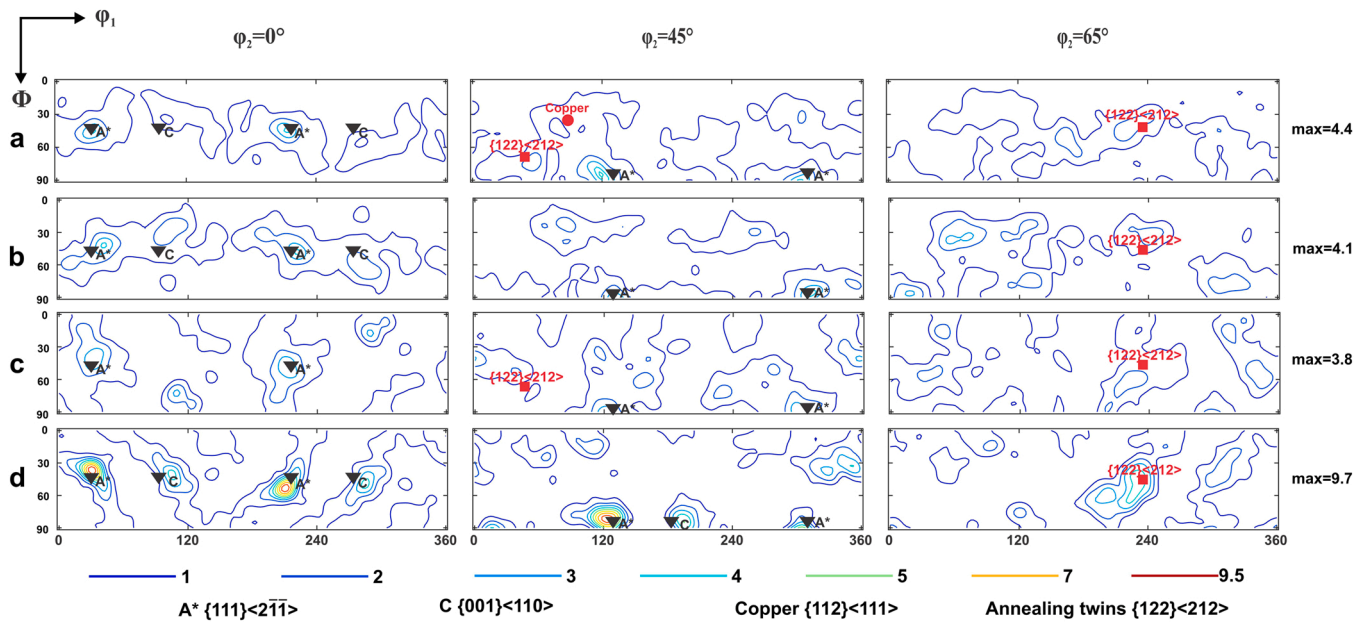**Fig. 11.** ODF sections ($\varphi_2 = 0°$, 45° and 65°) after the tribological test a) CR, b) RX15, c) RX30, d) RX45. Identification of shear components according to [63–65].
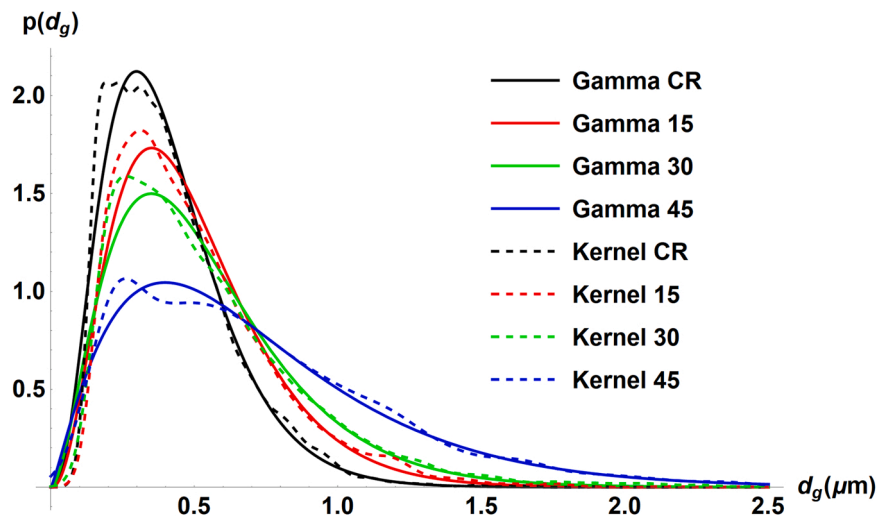

Fig. 12. Grain size distribution after the tribological test obtained by either using a smooth kernel distribution or fitting the CDF of the gamma distribution to the empirical CDF for CR, RX 15, RX 30 and RX 45.

- The paper presents significant new results as compared to a previous paper by the authors (Figueroa, et al. 2018. Mater. Char., 138, pp.263-273.), which focused only on the micromechanisms of tribolayer formation, while the present one puts a stronger focus on the tribological aspects and analyses the relationship between friction coefficient, surface deformation mechanisms during sliding wear and the mechanical properties of a ductile material after various annealing times

Declaration of Competing Interest

The authors declare that they have no known competing financial interests or personal relationships that could have appeared to influence the work reported in this paper.

Data Availability

Data will be made available on request.

References

[1] Smallman RE, Lee CS. Advances in the theory of deformation and recrystallization texture formation. Mater Sci Eng A 1994;184:97–112. https://doi.org/10.1016/0921-5093(94)91024-3.

[2] Humphreys FJ, Hatherly M. Recrystallization and related annealing phenomena. Elsevier; 2012.

[3] Doherty RD, Hughes DA, Humphreys FJ, Jonas JJ, Juul Jensen D, Kassner ME, et al. Current issues in recrystallization: a review. Mater Today 1998;1:14–5. https://doi.org/10.1016/S1369-7021(98)80046-1.

[4] Figueroa CG, Schouwenaars R, Cortés-Pérez J, Petrov R, Kestens L. Ultrafine gradient microstructure induced by severe plastic deformation under sliding contact conditions in copper. Mater Charact 2018:138. https://doi.org/10.1016/j.matchar.2018.02.017.

[5] Figueroa C.G., Ortega I., Jacobo V.H., Ortiz A., Bravo A.E., Schouwenaars R. Microstructures of tribologically modified surface layers in two-phase alloys. IOP Conf. Ser. Mater. Sci. Eng., vol. 63, 2014. https://doi.org/10.1088/1757–899X/63/1/012018.

[6] Figueroa C, Schouwenaars R, Jacobo V, Ortiz A, Petrov R, Kestens L. Tribological and microstructural characterization of ultrafine layers induced by wear in ductile alloys. Tribol Online 2016:11. https://doi.org/10.2474/trol.11.389.

[7] Figueroa CG, Jacobo VH, Ortiz A, Schouwenaars R. Critical analysis of a coaxial configuration for the characterization of adhesive wear and its application to Al and Al-Sn alloys. Tribol Lett 2015:59. https://doi.org/10.1007/s11249-015-0548-8.

[8] Aghababaei R, Warner DH, Molinari J-F. Critical length scale controls adhesive wear mechanisms. Nat Commun 2016;7:11816. https://doi.org/10.1038/ncomms11816.

[9] Kato K., Adachi K. Wear Mechanisms. Chapter 7 of Modern Tribology Handbook, Ed. B. Bhushan 2001.

[10] Challen JM, Oxley PLB. An explanation of the different regimes of friction and wear using asperity deformation models. Wear 1979;53:229–43. https://doi.org/10.1016/0043-1648(79)90080-2.

[11] Johnson KL. Contact mechanics. Cambridge University Press; 1989. https://doi.org/10.1201/b17588-12.

[12] Rigney DA, Chen LH, Naylor MGS, Rosenfield AR. Wear processes in sliding systems. Wear 1984;100:195–219. https://doi.org/10.1016/0043-1648(84)90013-9.

[13] Rigney DA. Transfer, mixing and associated chemical and mechanical processes during the sliding of ductile materials. Wear 2000;245:1–9. https://doi.org/10.1016/S0043-1648(00)00460-9.

[14] Rigney DA. Comments on the sliding wear of metals. Tribol Int 1997;30:361–7. https://doi.org/10.1016/S0301-679X(96)00065-5.

[15] Archard JF. Contact and rubbing of flat surfaces. J Appl Phys 1953;24:981–8. https://doi.org/10.1063/1.1721448.

[16] Hutchings IM. Wear and Lubrication. In: Buschow KHJ, Cahn RW, Flemings MC, Ilschner B, Kramer EJ, Mahajan S, et al., editors., Oxford: Elsevier; 2001, p. 9551–6. https://doi.org/https://doi.org/10.1016/B0–08-043152–6/01728–9.

[17] Rainforth WM. Microstructural evolution at the worn surface: a comparison of metals and ceramics. Wear 2000;245:162–77. https://doi.org/10.1016/S0043-1648(00)00476-2.

[18] Toth LS, Gu C. Ultrafine-grain metals by severe plastic deformation. Mater Charact 2014;92:1–14. https://doi.org/10.1016/j.matchar.2014.02.003.

[19] Valiev RZ, Islamgaliev RK, Alexandrov IV. Bulk nanostructured materials from severe plastic deformation. Prog Mater Sci 2000;45:103–89. https://doi.org/10.1016/S0079-6425(99)00007-9.

[20] Bagherpour E, Pardis N, Reihanian M, Ebrahimi R. An overview on severe plastic deformation: research status, techniques classification, microstructure evolution, and applications. Int J Adv Manuf Technol 2019;100:1647–94. https://doi.org/10.1007/s00170-018-2652-z.

[21] Valiev RZ, Estrin Y, Horita Z, Langdon TG, Zechetbauer MJ, Zhu YT. Producing bulk ultrafine-grained materials by severe plastic deformation. JOM 2006;58:33–9. https://doi.org/10.1007/s11837-006-0213-7.

[22] Wang PF, Han Z, Lu K. Enhanced tribological performance of a gradient nanostructured interstitial-free steel. Wear 2018;402–403:100–8. https://doi.org/10.1016/j.wear.2018.02.010.

[23] Schouwenaars R, Jacobo VH, Ortiz A. Microstructural aspects of wear in soft tribological alloys. Wear 2007;263:727–35. https://doi.org/10.1016/j.wear.2006.12.037.

[24] Moshkovich A, Perfilyev V, Lapsker I, Rapoport L. Friction, wear and plastic deformation of Cu and α/β brass under lubrication conditions. Wear 2014;320:34–40. https://doi.org/10.1016/j.wear.2014.08.016.

[25] Moshkovich A, Lapsker I, Feldman Y, Rapoport L. Severe plastic deformation of four FCC metals during friction under lubricated conditions. Wear 2017;386–387:49–57. https://doi.org/10.1016/j.wear.2017.05.018.

[26] Rigney DA, Naylor MGS, Divakar R, Ives LK. Low energy dislocation structures caused by sliding and by particle impact. Mater Sci Eng 1986;81:409–25. https://doi.org/10.1016/0025-5416(86)90279-X.

[27] Kapoor A, Johnson KL. Plastic ratchetting as a mechanism of metallic wear. Proc R Soc Lond Ser A Math Phys Sci 1994;445:367–84. https://doi.org/10.1098/rspa.1994.0066.

[28] Kapoor A. Wear by plastic ratchetting. Wear 1997;212:119–30. https://doi.org/10.1016/S0043-1648(97)00083-5.

[29] Kapoor A, Franklin FJ. Tribological layers and the wear of ductile materials. Wear 2000;245:204–15. https://doi.org/10.1016/S0043-1648(00)00480-4.

[30] Meshi L, Samuha S, Cohen SR, Laikhtman A, Moshkovich A, Perfilyev V, et al. Dislocation structure and hardness of surface layers under friction of copper in different lubricant conditions. Acta Mater 2011;59:342–8. https://doi.org/10.1016/j.actamat.2010.09.038.

[31] Archard JF, Hirst W, Allibone TE. The wear of metals under unlubricated conditions. Proc R Soc Lond Ser A Math Phys Sci 1956;236:397–410. https://doi.org/10.1098/rspa.1956.0144.

[32] Farhat ZN, Ding Y, Northwood DO, Alpas AT. Effect of grain size on friction and wear of nanocrystalline aluminum. Mater Sci Eng A 1996;206:302–13. https://doi.org/10.1016/0921-5093(95)10016-4.

[33] La P, Ma J, Zhu YT, Yang J, Liu W, Xue Q, et al. Dry-sliding tribological properties of ultrafine-grained Ti prepared by severe plastic deformation. Acta Mater 2005;53:5167–73. https://doi.org/10.1016/j.actamat.2005.07.031.

[34] Li WL, Tao NR, Han Z, Lu K. Comparisons of dry sliding tribological behaviors between coarse-grained and nanocrystalline copper. Wear 2012;274–275:306–12. https://doi.org/10.1016/j.wear.2011.09.010.

[35] Cui ZD, Zhu SL, Man HC, Yang XJ. Microstructure and wear performance of gradient Ti/TiN metal matrix composite coating synthesized using a gas nitriding technology. Surf Coat Technol 2005;190:309–13. https://doi.org/10.1016/j.surfcoat.2004.02.012.

[36] Peng R, Fu L, Zhou L. Improved wear resistance by phase transformation of surface nanocrystalline 1090 steel prepared by sandblasting technique. Appl Surf Sci 2016;388:406–11. https://doi.org/10.1016/j.apsusc.2015.12.010.

[37] Liu YJ, Liu Z, Jiang Y, Wang GW, Yang Y, Zhang LC. Gradient in microstructure and mechanical property of selective laser melted AlSi10Mg. J Alloy Compd 2018;735:1414–21. https://doi.org/10.1016/j.jallcom.2017.11.020.

[38] Mao X, Sun J, Feng Y, Zhou X, Zhao X. High-temperature wear properties of gradient microstructure induced by ultrasonic impact treatment. Mater Lett 2019;246:178–81. https://doi.org/10.1016/j.matlet.2019.03.059.

[39] Maki K, Ito Y, Matsunaga H, Mori H. Solid-solution copper alloys with high strength and high electrical conductivity. Scr Mater 2013;68:777–80. https://doi.org/10.1016/j.scriptamat.2012.12.027.

[40] Bravo AE, Durán HA, Jacobo VH, Ortiz A, Schouwenaars R. Towards new formulations for journal bearing alloys. Wear 2013;302:1528–35. https://doi.org/10.1016/j.wear.2013.01.040.

[41] Yasar I, Canakci A, Arslan F. The effect of brush spring pressure on the wear behaviour of copper–graphite brushes with electrical current. Tribol Int 2007;40:1381–6. https://doi.org/10.1016/j.triboint.2007.03.005.

[42] Standard A. E8/E8M-13a. Stand Test Methods Tens Test Met Mater ASTM Int West Conshohocken, PA 2013.

[43] Montgomery DC. Design and analysis of experiments. John Wiley & Sons; 2017.

[44] Figueroa CG, Garcia-Castillo FN, Jacobo VH, Cortés-Pérez J, Schouwenaars R. Microstructural and superficial modification in a Cu-Al-Be shape memory alloy due to superficial severe plastic deformation under sliding wear conditions. IOP Conf Ser Mater Sci Eng 2017;194. https://doi.org/10.1088/1757-899X/194/1/012011.

[45] Figueroa CG, Jacobo VH, Cortés-Pérez J, Schouwenaars R. Surface nanostructuring of a CuAlBe shape memory alloy produces a 10.3 ± 0.6 GPa nanohardness martensite microstructure. Materials 2020:13. https://doi.org/10.3390/ma13245702.

[46] Williams JA. Wear modelling: analytical, computational and mapping: a continuum mechanics approach. Wear 1999;225–229:1–17. https://doi.org/10.1016/S0043-1648(99)00060-5.

[47] Villaggio P. Wear of an elastic block. Meccanica 2001;36:243–250.

[48] Reye T. Zur theorie der zapfenreibung. Der Civ 1860;4:235–55.

[49] Scherge M, Shakhvorostov D, Pöhlmann K. Fundamental wear mechanism of metals. Wear 2003;255:395–400.

[50] Shakhvorostov D, Pöhlmann K, Scherge M. An energetic approach to friction, wear and temperature. Wear 2004;257:124–30. https://doi.org/10.1016/j.wear.2003.10.010.

[51] Tabor D. The hardness of metals. Oxford University Press; 2000.

[52] Bachmann F, Hielscher R, Schaeben H. Texture analysis with MTEX – free and open source software toolbox. Solid State Phenom 2010;160:63–8. https://doi.org/10.4028/www.scientific.net/SSP.160.63.

[53] Standard A. Standard test methods for determining average grain size. ASTM Stand E112–10 2013.

[54] Sheather SJ, Jones MC. A reliable data-based bandwidth selection method for kernel density estimation. J R Stat Soc Ser B 1991;53:683–90.

[55] Schouwenaars R, Van Houtte P. Methods for determining small differences between measured textures (Trans Tech Publ) Mater Sci Forum 2007;157:439–46.

[56] Hutchinson W.B., Lindh E., Bate P. On the determination of textures from discrete orientation measurements. (ICOTOM 12) 12 th Int. Conf. Textures Mater., 1999, p. 34–9.

[57] Liu Q, Juul Jensen D, Hansen N. Effect of grain orientation on deformation structure in cold-rolled polycrystalline aluminium. Acta Mater 1998;46:5819–38. https://doi.org/10.1016/S1359-6454(98)00229-8.

[58] Valiev RZ, Islamgaliev RK, Alexandrov IV. Bulk nanostructured materials from severe plastic deformation. Prog Mater Sci 2000;45:103–89. https://doi.org/10.1016/S0079-6425(99)00007-9.

[59] Chen X, Han Z. A low-to-high friction transition in gradient nano-grained Cu and Cu-Ag alloys. Friction 2021;9:1558–67.

[60] Belyakov A, Sakai T, Miura H, Tsuzaki K. Grain refinement in copper under large strain deformation. Philos Mag A 2001;81:2629–43. https://doi.org/10.1080/01418610108216659.

[61] Wang YM, Chen MW, Sheng HW, Ma E. Nanocrystalline grain structures developed in commercial purity Cu by low-temperature cold rolling. J Mater Res 2002;17:3004–7. https://doi.org/10.1557/jmr.2002.0436.

[62] Wang K, Tao NR, Liu G, Lu J, Lu K. Plastic strain-induced grain refinement at the nanometer scale in copper. Acta Mater 2006;54:5281–91. https://doi.org/10.1016/j.actamat.2006.07.013.

[63] Montheillet F, Cohen M, Jonas JJ. Axial stresses and texture development during the torsion testing of Al, Cu and α-Fe. Acta Met 1984;32:2077–89. https://doi.org/10.1016/0001-6160(84)90187-1.

[64] Enikeev NA, Schafler E, Zehetbauer MJ, Alexandrov IV, Valiev R. Observations of texture in large scale HPT-Processed Cu (Trans Tech Publ) Mater Sci Forum 2008; vol. 584:367–74.

[65] Suwas S, Ray RK. Crystallographic texture of materials. Springer-Verlag; 2014.

[66] Panin V, Kolubaev A, Tarasov S, Popov V. Subsurface layer formation during sliding friction. Wear 2001;249:860–7. https://doi.org/10.1016/S0043-1648(01)00819-5.

[67] Farhat ZN. Contribution of crystallographic texturing to the sliding friction behaviour of fcc and hcp metals. Wear 2001;250:401–8. https://doi.org/10.1016/S0043-1648(01)00604-4.

[68] Cai W, Mabon J, Bellon P. Crystallographic textures and texture transitions induced by sliding wear in bronze and nickel. Wear 2009;267:485–94. https://doi.org/10.1016/j.wear.2008.11.016.

[69] Cai W, Bellon P. Effect of annealing treatment on the dry sliding wear behavior of copper. Wear 2019;426–427:1187–94. https://doi.org/10.1016/j.wear.2019.01.014.

[70] Dryzek J, Wróbel M. Detection of tribolayer in pure iron using positron annihilation and EBSD techniques. Tribology Int 2020;144:106133. https://doi.org/10.1016/j.triboint.2019.106133.

[71] Van Houtte P, Aernoudt E. Considerations on the crystal and the strain symmetry in the calculation of deformation textures with the taylor theory. Mater Sci Eng 1976;23:11–22. https://doi.org/10.1016/0025-5416(76)90082-3.

[72] Kocks UF, Tomé CN, Wenk H-R. Texture and anisotropy: preferred orientations in polycrystals and their effect on materials properties. Cambridge University Press; 2000.

[73] Al-Fadhalah KJ, Alhajeri SN, Almazrouee AI, Langdon TG. Microstructure and microtexture in pure copper processed by high-pressure torsion. J Mater Sci 2013;48:4563–72. https://doi.org/10.1007/s10853-013-7200-5.

[74] Naghdy S, Kestens L, Hertelé S, Verleysen P. Evolution of microstructure and texture in commercial pure aluminum subjected to high pressure torsion processing. Mater Charact 2016;120:285–94. https://doi.org/10.1016/j.matchar.2016.09.012.

[75] Jahedi M, Beyerlein IJ, Paydar MH, Knezevic M. Effect of grain shape on texture formation during severe plastic deformation of pure copper. Adv Eng Mater 2018;20:1600829. https://doi.org/10.1002/adem.201600829.

[76] Li S, Beyerlein IJ, Alexander DJ. Characterization of deformation textures in pure copper processed by equal channel angular extrusion via route A. Mater Sci Eng A 2006;431:339–45. https://doi.org/10.1016/j.msea.2006.06.022.

[77] Xue Q, Beyerlein IJ, Alexander DJ, Gray GT. Mechanisms for initial grain refinement in OFHC copper during equal channel angular pressing. Acta Mater 2007;55:655–68. https://doi.org/10.1016/j.actamat.2006.08.049.

[78] Rabinowicz E. The determination of the compatibility of metals through static friction tests. A S L E Trans 1971;14:198–205. https://doi.org/10.1080/05698197108983243.

[79] Guo Y, Compton WD, Chandrasekar S. In situ analysis of flow dynamics and deformation fields in cutting and sliding of metals. Proc R Soc A Math Phys Eng Sci 2015;471:20150194.

[80] Mahato A, Guo Y, Sundaram NK, Chandrasekar S. Surface folding in metals: a mechanism for delamination wear in sliding. Proc R Soc A Math Phys Eng Sci 2014;470:20140297.

[81] Sundaram NK, Guo Y, Chandrasekar S. Mesoscale folding, instability, and disruption of laminar flow in metal surfaces. Phys Rev Lett 2012;109:106001.

[82] Pouryazdan M, Kaus BJP, Rack A, Ershov A, Hahn H. Mixing instabilities during shearing of metals. Nat Commun 2017;8:1–7.

[83] Beckmann N, Romero PA, Linsler D, Dienwiebel M, Stolz U, Moseler M, et al. Origins of folding instabilities on polycrystalline metal surfaces. Phys Rev Appl 2014;2:64004.

[84] Argibay N, Chandross M, Cheng S, Michael JR. Linking microstructural evolution and macro-scale friction behavior in metals. J Mater Sci 2017;52:2780–99. https://doi.org/10.1007/s10853-016-0569-1.

[85] Grützmacher P, Gachot C, Eder SJ. Visualization of microstructural mechanisms in nanocrystalline ferrite during grinding. Mater Des 2020;195:109053. https://doi.org/10.1016/j.matdes.2020.109053.

[86] Eder SJ, Grützmacher PG, Rodríguez Ripoll M, Dini D, Gachot C. Effect of temperature on the deformation behavior of copper nickel alloys under sliding. Materials 2021;4:60–5. https://doi.org/10.3390/ma14010060.